Experiments in Fluids (2023) 64:122
https://doi.org/10.1007/s00348-023-03647-2

RESEARCH ARTICLE

Profiles of streamwise velocity and fluctuations in a hypersonic turbulent boundary layer using acetone tagging velocimetry

Ben A. Segall[1] · David Shekhtman[1] · Ahsan Hameed[1] · James H. Chen[1] · Nicholaus J. Parziale[1]

Received: 9 February 2023 / Revised: 19 April 2023 / Accepted: 23 April 2023 / Published online: 13 June 2023

Abstract

Acetone tagging velocimetry (ATV) with nominally 1% mole fraction acetone seeding was conducted in a shock-tunnel-generated hypersonic turbulent boundary layer over a hollow-cylinder-flare at $M_e = 6.05$, $T_w/T_r = 0.65$, $\mathrm{Re}_\theta = 8925$, and $\mathrm{Re}_\tau = 408$. This single-laser tagging velocimetry experiment measured streamwise velocity and fluctuations, $\overline{u}$ and u'_{RMS}, had a repetition rate of 50 kHz, and did not require the use of an image intensifier. The ATV data are non-dimensionalized via the van Driest transformation and compares well with the literature down to $y^+ \approx 3$; this is into the viscous sublayer. The Morkovin-scaled fluctuations matched the literature for $y^+ > 10$; however, below $y^+ \approx 10$, it appears that the noise introduced by the measurement technique, in addition to the velocity differences being small near the wall, rendered the ATV-measured Morkovin-scaled fluctuations below $y^+ = 10$ not useful.

1 Introduction

High-speed vehicle design requires a reasonably accurate prediction of the skin friction and heat transfer (Leyva 2017). The state of the boundary layer on such vehicles is often turbulent which necessitates accurate reduced-order turbulence models (ROMS), such as the Reynolds-averaged Navier–Stokes (RANS) approach, because the length and time scales of such flows are too widespread to be solved with direct numerical simulation (DNS). It is a requirement that models like RANS have to be verified over canonical geometries before they may be applied to more complex vehicle designs (Holden et al. 2013, 2014). Thus, there is a need to develop advanced laser diagnostics to probe these complex flows (Danehy et al. 2018; Jiang et al. 2023).

✉ Nicholaus J. Parziale
nick.parziale@gmail.com

Ben A. Segall
bsegall@stevens.edu

David Shekhtman
davshe98@gmail.com

Ahsan Hameed
ahameed@stevens.edu

James H. Chen
jchen101@stevens.edu

[1] Mechanical Engineering, Stevens Institute of Technology, 1 Castle Point, Hoboken, NJ 07030, USA

The specific motivation of this paper is to address the dearth of turbulence quantity measurements that support high-speed turbulence models. Examples of existing experiments are those by Laderman and Demetriades (1974) (hotwire), Brooks et al. (2017, 2018) (PIV), Williams et al. (2018) (PIV), and Neeb et al. (2018) (PIV). Streamwise velocity and fluctuations from these experiments and DNS appear to compare reasonably well. However, wall-normal velocity fluctuation measurements from these experiments do not match predictions from DNS, nor do they have a sufficient near-wall resolution ($y^+ < 30$). The mismatch from DNS is an ambiguity that must be rectified because the DNS predictions are an as-yet unvalidated data set and the PIV measurements are thought to potentially suffer from particle-lag (Aultman et al. 2022) at high Knudsen number (Loth 2008) which essentially acts like a low-pass filter to the data Brooks et al. (2017, 2018). Tagging Velocimetry (TV), which is reviewed in Tropea et al. (2007); Danehy et al. (2018); Jiang et al. (2023), has been proposed as a non-intrusive diagnostic in the hypersonic flow regime to provide off-surface, time-of-flight velocity profile measurements that do not suffer from particle lag issues. The long-term goal with TV is to make time-resolved simultaneous measurements of streamwise and wall-normal velocity and fluctuations.

Several popular tracers used for TV include krypton (Parziale et al. 2015; Zahradka et al. 2016; Mustafa and Parziale 2017, 2017a; Mustafa et al. 2017b , 2018; Mustafa

and Parziale 2018; Mustafa et al. 2019a, b; Shekhtman et al. 2020, 2021; Jiang et al. 2023), oxygen (Clark et al. 2022), biacetyl (Mirzaei et al. 2012), hydroxyl (Boedeker 1989; Wehrmeyer et al. 1999; Pitz et al. 2005; Andre et al. 2017), iodine (McDaniel et al. 1983; Balla 2013), nitric oxide (Danehy et al. 2003), nitrogen (Michael et al. 2011; Edwards et al. 2015; Jiang et al. 2016, 2017), and argon (Mills 2016) as well as many others.

Acetone as a tracer for tagging velocimetry is the subject of ongoing research. Initially recognized for its use in planar laser-induced fluorescence (PLIF), acetone is readily available and inexpensive, and the excitation spectrum is accessible by the fourth harmonic of an Nd:YAG laser, which is 266 nm light (Lozano 1992; Handa et al. 2011; Fratantonio et al. 2018). A review of the complex photophysics of acetone can be found in Blitz et al. (2006). Additionally, the discussion in Sect. 4 of Lempert et al. (2003) explains the subtle difference between the fluorescence, which has a decay time of $\approx 1\,\mu$s, and phosphorescence, which has a decay time of $\approx 1000\,\mu$s. Additional research on the photophysics of acetone can be found in Schulz and Sick (2005); Tran et al. (2005); Tran (2008); Fratantonio et al. (2018), among others.

Acetone tagging velocimetry (ATV) with a 266 nm laser was demonstrated by Lempert et al. (2002, 2003) in an acetone-seeded nitrogen jet with a 250–500 ns write/read delay time and a camera gate of 20 ns. Images were averaged over 3–10 s at a repetition rate of 10 Hz. Handa et al. (2014) used ATV to study supersonic rectangular microjets using a 20 ns gate and a 300–900 ns write/read delay. Gragston and Smith (2022) performed acetone tagging at 10 kHz in acetone-seeded air to probe the freestream and turbulent boundary layer of the test section of the UTSI Mach 4 Ludwieg Tube. Interframe times are 10−16.7 µs, and gate width is not reported. Andrade et al. (2022) performed 10 kHz acetone tagging of acetone-seeded nitrogen gas flows in the freestream and test section wall of the UT Mach 7 Ludwieg Tube Wind Tunnel using a gate of 1 µs and an effective interframe time of longer than 15 µs; the interframe time in that work is inferred from the line displacement and edge velocity.

In this paper, we discuss the experimental approach as applied to Mach 6 turbulent boundary-layer flow over a hollow-cylinder flare (HCF). We report the turbulent boundary-layer profiles of streamwise velocity and fluctuations, u down to a $y^+ \approx 3$ and u' down to $y^+ \approx 10$, which appear to be some of the first such measurements in the literature in hypersonic, turbulent flows using the TV technique. These data are then non-dimensionalized and compared to literature with favorable agreement.

2 Experimental setup

2.1 Ground-test facility and run conditions

The Stevens Shock Tunnel (Fig. 1) was designed to replicate Mach 6 free-flight flow conditions with an enthalpy of 1.5 MJ/kg and a unit Reynolds number of up to $\mathrm{Re}^u_\infty = 8 \times 10^6\ \mathrm{m}^{-1}$ for at least 5 ms when using helium as a driver gas and air or N_2 as the driven (test) gas (Shekhtman et al. 2022). Using nitrogen as the driver gas and air/N_2 as the driven (test) gas with a pressure ratio of 10, the enthalpy in the nozzle reservoir is typically ≈ 0.5 MJ/kg and offers a test time of 12-15 ms and up to $\mathrm{Re}^u_\infty = 32 \times 10^6\ \mathrm{m}^{-1}$. For this campaign, we choose the ≈ 0.5 MJ/kg condition at $\mathrm{Re}^u_\infty = 16 \times 10^6\ \mathrm{m}^{-1}$ because of the relatively high Reynolds number and modest reservoir temperature ($T_R = 500$ K) which precludes the breakdown of acetone in the reservoir (details of this assertion follow). In the current configuration, we have a double-diaphragm separating the driver section (5.0 m long), and the driven section (11.07 m long), both of which have a 194 mm inner diameter. The nozzle exit diameter is 406 mm with a core of approximately 330 mm. The hollow-cylinder flare (HCF) test article fits within the inviscid test rhombus, as shown in Fig. 2. The HCF is 1 m-long with a 0.102 m outer diameter hollow cylinder and a 34° flare of maximum diameter 0.203 m. A 0.15 m (6 in) long trip

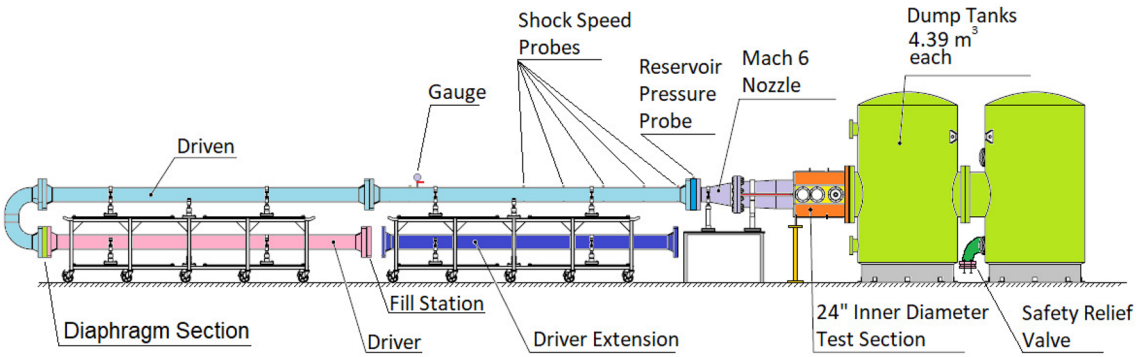

Fig. 1 Schematic of Stevens Shock Tunnel. Drawing to scale. Scale is driver tube is 5 m

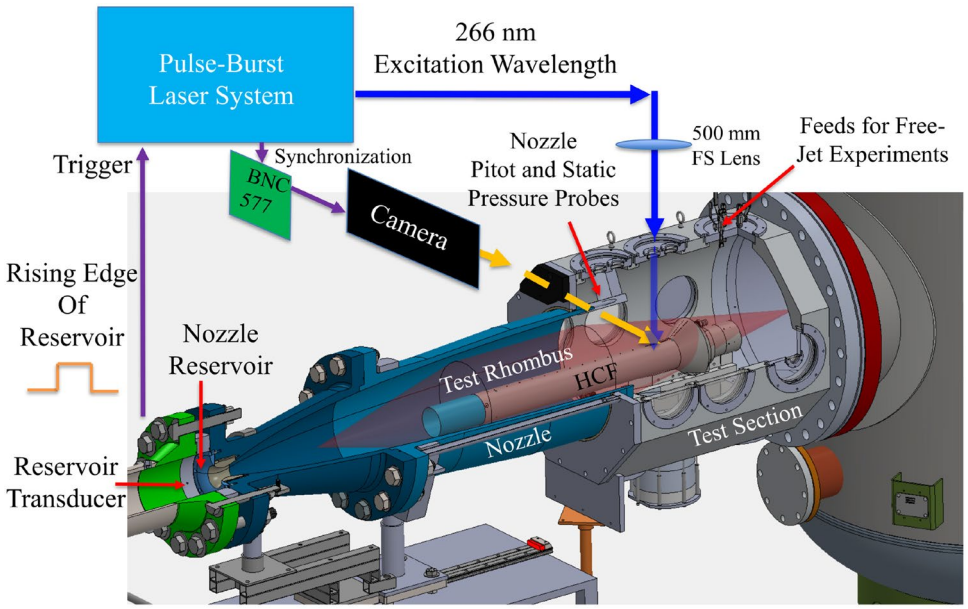

Fig. 2 Experimental Approach for Tagging Velocimetry in the Stevens Shock Tunnel. Diagram of setup

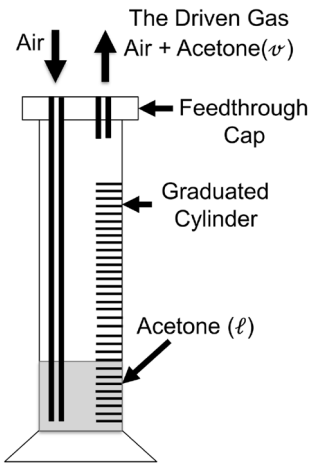

Fig. 3 Schematic of Acetone Bubbler

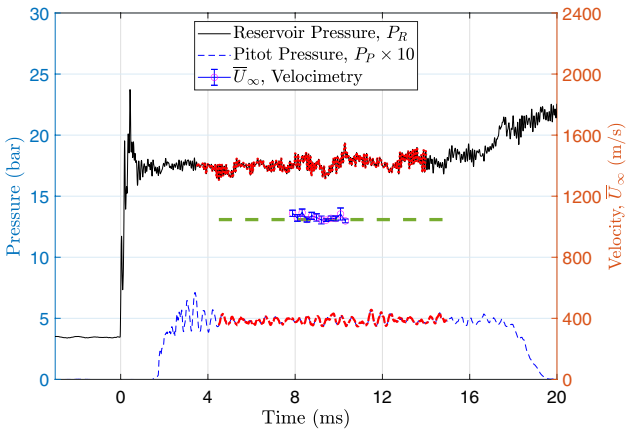

Fig. 4 Pressure Traces and Freestream Velocimetry Data for Shot 270. Test times are indicated by a thick red lineweight. Run conditions are listed in Table 1

composed of 50 grit sanding belt was placed 0.26 m (10 in) from the sharp leading edge to induce turbulence.

Acetone vapor was seeded into air as the driven-section test gas via a bubbler, which consisted of a capped graduated cylinder as shown in Fig. 3. The graduated cylinder was used to measure the volume of liquid acetone before and after the filling process to determine the mass of acetone vapor in the driven gas. Given the acetone mass and the composition of air, a fixed-point iteration method using Cantera (Goodwin 2003) was used to calculate the mole fraction of acetone in the test gas. Run conditions are shown in Table 1. Reservoir conditions were calculated with both Cantera and the Shock and Detonation Toolbox (Browne et al. 2006). The appropriate thermodynamic data are found in the literature (Gordon and McBride 1999; McBride et al. 2002).

Freestream conditions were calculated via the method described in Mustafa et al. (2017) and Korte et al. (2021), utilizing reservoir and Pitot pressure traces and assuming an isentropic expansion to iteratively find freestream Mach number M_∞. In Fig. 4, we show representative reservoir and Pitot-pressure traces as well as the freestream velocity as measured at the boundary-layer edge with ATV. The freestream velocity measurements compare well with the calculated velocity denoted by a dashed green line, bringing confidence to the run-condition calculations. To assess model alignment, static pressure on the surface of

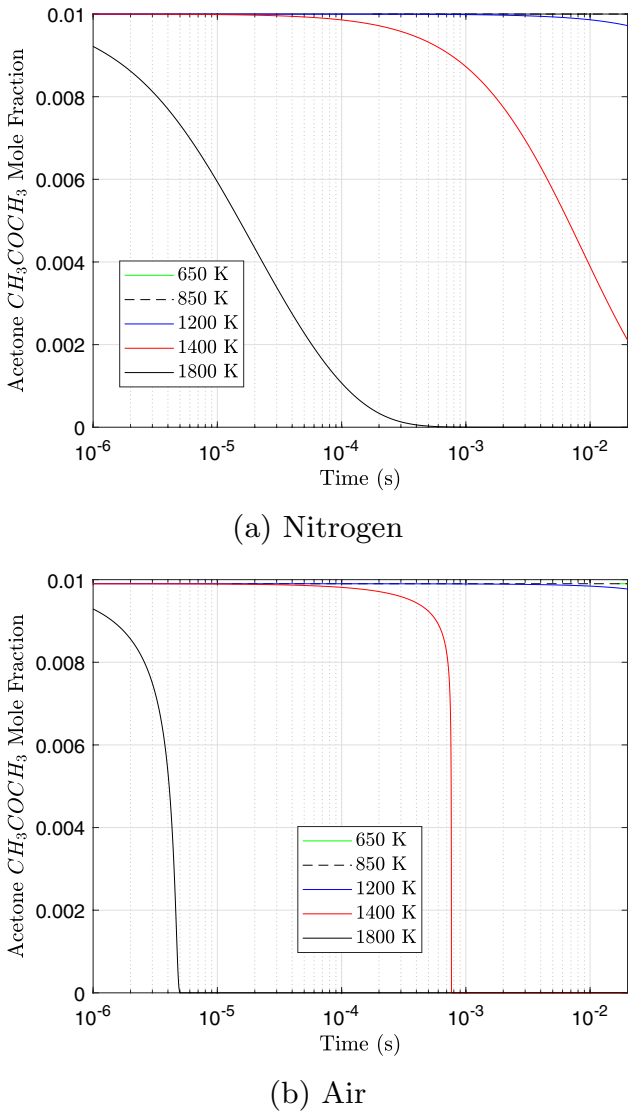

Fig. 5 Acetone Mole Fraction versus Time in seeded Nitrogen (**a**) and Air (**b**)

the cylinder at azimuthal angles of 60 and 300 degrees at $x = 0.100$ mm and 0, 120, and 240 degrees at $x = 0.600$ mm. These measurements were all within 3% bringing confidence to model alignment in the test section and flow uniformity.

Of concern during this campaign was the degree to which the acetone would pyrolyze and react with the test gas. Using nitrogen as the driver gas and a pressure ratio of 10, the reservoir temperature is typically $T_R \approx 500$ K. Sato and Hidaka (2000) found that at a steady state temperature exceeding 573 K, acetone will pyrolyze, which in the present experiments would complicate reservoir-condition calculation and potentially reduce tracer signal. However, the risk of acetone pyrolysis is reduced considerably by the short run times of the tunnel ($\approx$ 20 ms). To investigate this, we perform a kinetics study assuming an initial acetone mole fraction of 0.01 with a mechanism from Yu et al. (2018). Results are presented for acetone-seeded air and nitrogen at various temperatures in Fig. 5. For temperatures below 1200 K for acetone-seeded nitrogen and air at pressure 3.5 MPa, there is little predicted acetone decomposition during the useful test time of the Stevens Shock Tunnel. Therefore, acetone-seeded air can be used for shock tunnel experiments in which the reservoir temperature does not exceed 1200 K, given a reservoir pressure of 3.5 MPa (500 psi). From this, we conclude that there is no appreciable acetone degradation in the reservoir for the current test campaign.

2.2 Experimental tagging velocimetry setup

The motivation of this work is to make high-fidelity observations of high-speed turbulence for comparison to computations. To design a relevant experiment, we must make estimates of the prominent scales in the flow, noting an approximate boundary-layer thickness of $\delta \approx 10$ mm, which was determined from the mean flow profile, and freestream velocity of $U_\infty \approx 1000$ m/s. As such, we estimate some large structures in the flow to have a timescale of $\tau_L \approx \delta / U_\infty \approx 10\,\mu$s. We aim to resolve structures of this timescale and smaller. This is why we choose the method of successive imaging of fluorescence of Lempert et al. (2002, 2003) and choose an write/read delay time of 450 ns with an exposure time of 95 ns. Due to Nyquist, the smallest turbulent time scale we can resolve is twice the 450 ns write/read delay time, resulting in a Nyquist frequency for each snapshot of approximately 1 MHz.

In contrast to other TV techniques, the laser and imaging setup is relatively simple. The imaging system consisted of a Phantom TMX 7510 with a 135 mm Carl Zeiss lens and a 20 mm lens tube to increase magnification. The image length scale is 15.0 pixels/mm. The camera was pulsed by a Berkeley Nucleonics Model 577 pulse/delay generator (PDG), which was triggered at 50 kHz by the QuasiModo Quantum Composer (a signal generator inside the laser), resulting in a frame rate of 50 kHz (20 µs between frames). The PDG synchronized the camera strobe (gate) using its duty-cycle feature, timing the capture of the write images at user-defined locations within a given pulse train. As shown in Fig. 6, one write image is captured at zero delay from a single 266 nm laser pulse. Then, ten consecutive read images are captured by gating the camera at a delay of 450 ns from ten respective laser pulses (the write/read delay time)—one laser pulse per read image. Then, the duty-cycle resets and one write image is captured at zero delay from a single 266 nm laser pulse and ten read images are captured at a delay of 450 ns from ten respective laser pulses, and so on.

As shown in Fig. 2, ATV experiments utilized an externally triggered Spectral Energies QuasiModo 1200 Burst-Mode Laser System, where we prescribe a 4 ms burst train duration, a repetition rate of 50 kHz, and a pulse duration

Table 1 Run Conditions, where P_4 is driver-section nitrogen gas pressure; P_4/P_1 is the driver-to-driven pressure ratio that determines the driven air gas pressure P_1; u_s is the shock speed; M_s is the shock Mach number; T_R is the reservoir temperature; P_R is the reservoir pressure; P_∞ is the freestream pressure, T_∞ is the freestream temperature, M_∞ is the freestream Mach number, U_∞ is the time-averaged freestream velocity, and Re^u_∞ is the unit Reynolds number

Shot	P_4 (MPa)	$\frac{P_4}{P_1}$	$X_{C_3H_6O}$	u_s (m/s)	M_s	P_R (MPa)	T_R (K)	P_∞ (kPa)	T_∞ (K)	M_∞	U_∞ (m/s)	Re^u_∞ (10^6 1/m)
270	3.44	10	0.0088	504	1.46	1.76	485	1.01	58.7	6.07	935	14.7
273	3.44	10	0.012	511	1.48	1.79	488	1.01	59.0	6.08	940	14.6
274	3.46	10	0.023	505	1.48	2.48	505	1.25	62.9	6.02	960	16.0
276	3.46	10	0.0079	528	1.52	2.11	516	1.25	62.9	6.04	964	16.1
280	3.45	10	0.015	500	1.46	2.17	510	1.21	61.9	6.08	962	16.1
282	3.45	10	0.015	510	1.48	2.12	509	1.26	62.9	6.02	960	16.2
Average	3.45	10	0.013	510	1.48	2.07	502	1.17	61.4	6.05	954	15.6

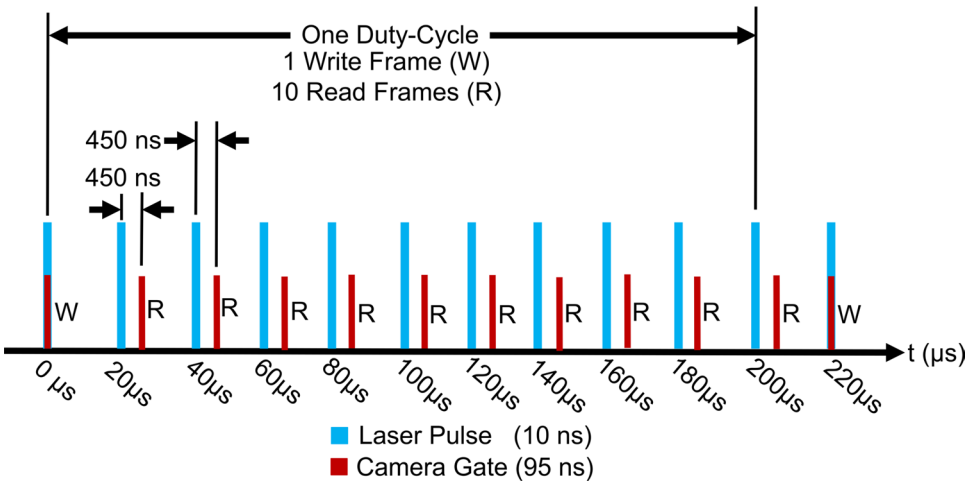

Fig. 6 Duty-cycle Timing Diagram

of 10 ns. The average pulse train energy was 7.75 J for 200 pulses at 266 nm, resulting in an average pulse energy of ≈ 38 mJ. Frequency conversion from the fundamental 1064 nm was performed with two successive frequency-doubling crystals built into the system. Of the 4 ms burst width, the laser generated sufficient intensity for ≈ 3 ms, which corresponds to 150 frames. During a test run, the start of the pulse burst train was triggered by the rising edge of a reservoir pressure transducer. At a prescribed delay (7.5 ms) from this rising edge, the burst-mode laser system pulses at the excitation wavelength into the test section (see the timing in Fig. 3). The pulse is directed toward the test section and is focused by an $f = 500$ mm plano-convex lens. The beam enters the test section through a 0.0254 m (1 in) diameter, 3 mm (0.12 in) thick fused-silica glass window.

The approach and coordinate transformation of Mustafa et al. (2019b) were implemented to interrogate the boundary layer. As shown in Fig. 7, the 266 nm excitation laser beam was oriented approximately tangential to the hollow cylinder portion of the test article, in a location upstream of the shock-wave/turbulent boundary-layer interaction to increase

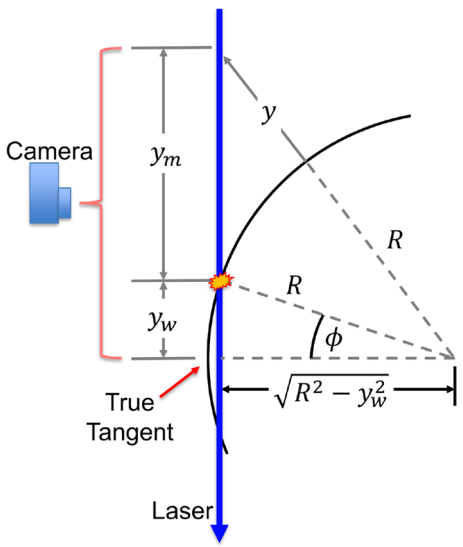

Fig. 7 Schematic that geometrically relates the image coordinate y_m to wall-normal coordinate y

wall resolution. The beam was focused to ≈ 68 µm near the true tangent of the cylinder. The spot size was determined to be diffraction limited, assuming $M^2 = 4$ (per manufacturer specification) for the 266 nm laser. By grazing the surface of the cylinder, the size of the laser-induced ablation plume at the wall was minimized. The probing location was 0.9 m (35.5 in) from the cylinder leading edge. Using Fig. 7 and the Pythagorean Theorem, a coordinate transformation between the measured image coordinate y_m to the wall-normal coordinate y was derived:

$$y = \sqrt{R_c^2 + y_m^2 + 2y_m y_w} - R_c, \tag{1}$$

where R_c is the radius of the hollow cylinder (0.0508 m) and y_w is the location of the no-slip condition from the true tangent of the cylinder, as seen by the camera.

3 Results

Acetone tagging results are presented for the shock tunnel experiments whose run conditions are listed in Table 1. Acetone mole fractions were 0.9–2.3%. A write/read delay time of 450 ns was used to allow sufficient displacement to capture the signal, observe structure, and minimize velocity measurement error. Sample processed images are shown in Fig. 8. Write and read images were processed as follows: (1) cropped to the region of interest; (2) smoothed via a Wiener Filter; (3) zeroed to the minimum value and normalized by the resulting image maximum value; (4) smoothed by 10 pixels across each row, and (5) processed via the peak-finding algorithm of OHaver (1997), which fits a Gaussian to the peak of each row.

The write lines were fitted to the write images which were recorded every 11 frames to monitor any displacement between the laser and the HCF during a run. These write lines are marked as W in Fig. 8. The read lines, marked as R, were extracted from the processed read images which were recorded 10 out of 11 frames. Also note that the y-coordinate in Fig. 8 is y_m in Fig. 7 prior to the scaling of Eq. (1). Profiles with velocity less than −1000 m/s and greater than +2000 m/s were removed from the ensuing analysis. These erroneous samples comprised less than 5% of the data. Rows of data and fits to that data processed via the peak-finding algorithm of OHaver (1997) for Shot 280 at 9.18 ms are presented in Fig. 9. Data at $y_m = 5.85$ mm and $y_m = 37.8$ mm represent data from the boundary layer and the freestream, respectively.

Error for the ATV measurements are calculated in the same fashion as Zahradka et al. (2016):

$$\widetilde{U} = \sqrt{\left(\widetilde{\Delta x}\frac{\partial U}{\partial \Delta x}\right)^2 + \left(\widetilde{\Delta t}\frac{\partial U}{\partial \Delta t}\right)^2 + \left(v'_{\mathrm{RMS}}\frac{\partial U}{\partial y}\Delta t\right)^2}, \tag{2}$$

where uncertainty estimates of a variable are indicated with a tilde. The uncertainty in the measured displacement distance, $\widetilde{\Delta x}$, of the tracer is estimated as 25 µ m from the 95% confidence bound on the write and read locations from

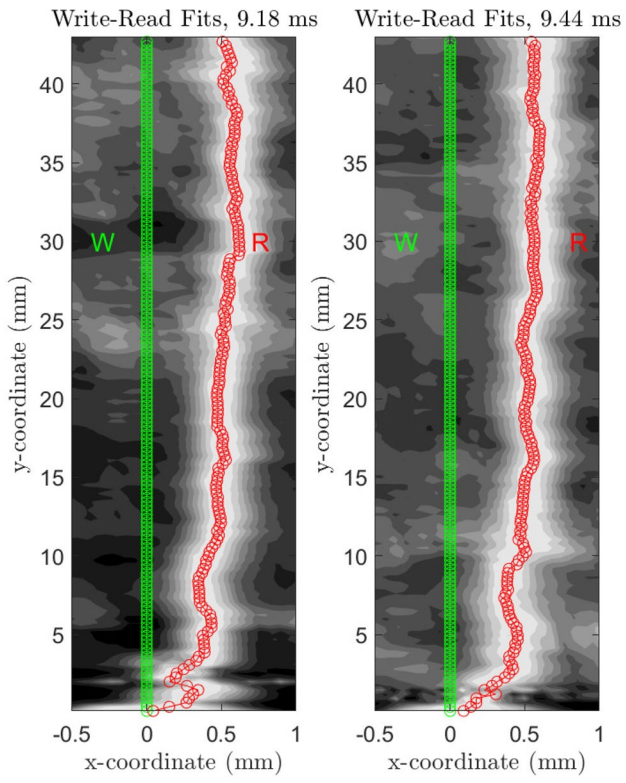

Fig. 8 Representative write- and read-frame fitting from Shot 280. The letters W and R indicate a write fit and a read fit, respectively. The y-coordinate is y_m in Fig. 7

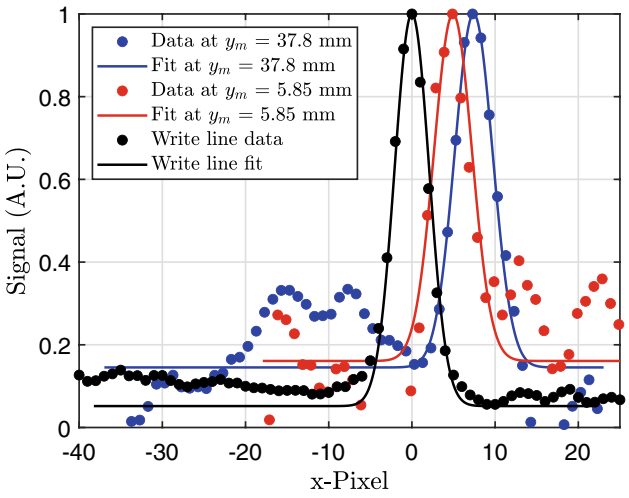

Fig. 9 Rows of data and fits for Shot 280 at 9.18 ms in Fig. 8. Data at $y_m = 5.85$ mm and $y_m = 37.8$ mm represent data from the boundary layer and the freestream, respectively

the Gaussian fits due to a bootstrap error analysis (OHaver 1997). This results in an estimated minimum resolvable velocity of $U_{\min} \approx 2\widetilde{\Delta x}/\Delta t \approx 100$ m/s, which is less than half of the minimum average velocity in Fig. 10. The uncertainty in time, $\widetilde{\delta t}$, is estimated to be half the camera gate width, 47.5 ns, which causes fluorescence blurring as considered in Bathel et al. (2011). The third term in Eq. (2) is uncertainty in streamwise velocity due to wall-normal flow in the xy-plane. This formulation is taken from Hill and Klewicki (1996) and Bathel et al. (2011). The wall-normal fluctuations used in Eq. (2) (v'_{RMS}) are conservatively estimated to be 10% of the edge velocity.

For a given experiment, 150 usable frames were recorded ($\approx$ 3 ms at 50 kHz). This limitation is imposed by concerns of burning optics in the laser or elsewhere if the pulse train were to be made longer. This is not sufficient to generate statistically significant mean and fluctuating boundary-layer profiles. As such, we repeat the same condition six times to generate sufficient realizations. In Fig. 10, profiles are plotted for the six experiments listed in Table 1. Of the six experiments performed, two experiments (Shot 270 and Shot 273) were unable to capture near-wall resolution due to laser-induced breakdown on the surface of the hollow cylinder. We believe that the noise from the relatively long-lived laser-induced breakdown was worse for the excluded two runs because the laser beam was not issued tangentially enough to the hollow cylinder; that is y_w in Fig. 7 was too large. We also note that Khalil et al. (2006) observed a similarly long $\approx$ 1 µs lifetime of stainless steel laser-induced breakdown. The average near-wall velocity profile data for the remaining four shots are plotted in red and includes 377 realizations while the blue line depicts the average profile for all six experiments and includes 555 realizations.

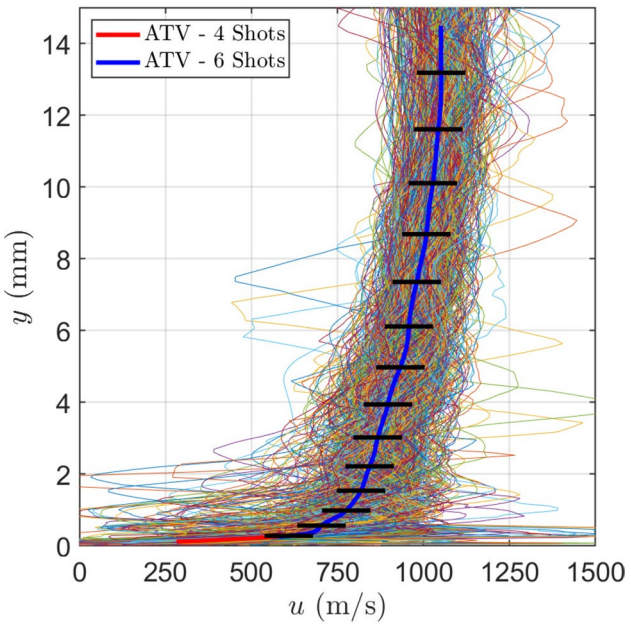

Fig. 10 All velocity profiles for all six experiments are plotted as thin multicolored lines. The mean velocity profile of all six experiments is blue and the red profile is a subset of four where we found sufficient near-wall SNR. Black error bars due to Eq. (2)

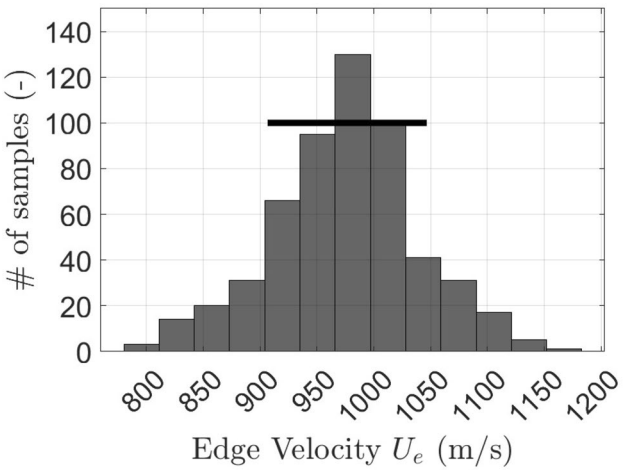

Fig. 11 Distribution of velocity at the boundary layer edge. Error bar is in black and corresponds to the boundary-layer edge in Fig. 10

To average the data for non-dimensionalization, there is a concern that the run conditions are disparate. In Fig. 11, a distribution of the velocity at the boundary-layer edge, U_e, is presented along with the computed error of mean velocity. The measured mean velocity is 975 ± 70 m/s (7%), which is well within the computed freestream velocity reported for any experiment in Table 1. This brings confidence to the run-condition calculation, as well as the presentation of an averaged run condition at the bottom of Table 1.

4 Discussion

In this section, the data are non-dimensionalized and compared to data from the literature. To compare data from separate shots where the run conditions were very similar but not identical, the data from each experiment is first non-dimensionalized and then the resulting non-dimensional data is averaged. Note that the alternative method of first averaging all the profiles and then performing the non-dimensionalization results in essentially the same figures. The averaged conditions are listed in the bottom row of Table 1 and, in an additional form, here in Table 2.

Table 2 Turbulence Quantities

M_e	T_w/T_r	Re_θ	Re_τ	$C_f \times 10^3$	u_τ (m/s)
6.05	0.65	8925	408	1.07	52.4

Following the formulation of Huang and Coleman (1994), the experimentally obtained velocity can be non-dimensionalized with the van Driest transformation as

$$U^+_{VD} = \frac{1}{R}\left[\sin^{-1}\frac{R(U^+ + H)}{D} - \sin^{-1}\left(\frac{RH}{D}\right)\right], \tag{3}$$

where $U^+ = u/u_\tau$, shear velocity $u_\tau = \sqrt{\tau_w/\rho_w}$, $H = B_q/[(\gamma-1)M_\tau^2]$, $R = M_\tau\sqrt{(\gamma-1)Pr_t/2}$, and $D = \sqrt{1+R^2H^2}$ with parameters defined as follows: $M_\tau = u_\tau/\sqrt{(\gamma-1)C_pT_w}$, heat transfer coefficient $B_q = q_w/(\rho_w C_p u_\tau T_w)$, and turbulent Prandtl number $P_t = 0.9$ (Danis and Durbin 2022). Here, u is the measured velocity, u' is the measured fluctuating velocity, q_w is the heat flux into the flow from the wall, ρ_w is the density of the gas at the wall, C_p is the constant pressure, mass-specific heat capacity, γ is the specific heat ratio, T_w is the wall temperature, and τ_w is the wall shear stress. The temperature profile is obtained via Walz's use (Walz 1959) of the Crocco–Busemann relation (White 2006) as

$$\overline{T} = T_w\left[1 + \left(\frac{T_r}{T_w} - 1\right)\frac{\overline{u}}{U_e} - \frac{\gamma-1}{2}M_e^2\left(\frac{T_e}{T_w}\right)\left(\frac{\overline{u}}{U_e}\right)^2\right], \tag{4}$$

where U_e is the edge velocity, T_e is the edge temperature, M_e is the edge Mach number, T_r is the recovery temperature

$$T_r = T_e\left[1 + \left(\frac{\gamma-1}{2}\right)rM_e^2\right], \tag{5}$$

and r is the recovery factor estimated to be $0.9 \approx Pr^{1/3}$. The mean density profile is determined as $\overline{\rho} = \rho_w T_w/\overline{T}$, assuming negligible wall-normal pressure gradient. Using the resulting mean density profile, $\overline{\rho}$, the momentum thickness Reynolds number is calculated to estimate a friction factor coefficient, C_f, from a compressibility-corrected friction factor correlation, which is then used to estimate wall shear stress $\tau_w = (1/2)\rho_e u_e^2 C_f$. Recent work by Huang et al. (2022) states that "[a]mong the various combinations of compressible transformations and incompressible correlations for the skin friction, the combination of van Driest II transformation with the power-law relation of Smits et al. (1983) correlates best with the DNS data" at Mach numbers and wall-temperature ratios similar to the present work. The Smits et al. (1983) compressibility-corrected friction factor is calculated as

$$C_f = \frac{1}{F_c}0.024(F_\theta \mathrm{Re}_\theta)^{-1/4}, \tag{6}$$

where the compressibility corrections are $F_\theta = \mu_e/\mu_w$ and

$$F_c = \frac{(\gamma-1)rM_e^2}{2(\sin^{-1}(\alpha) + \sin^{-1}(\beta))^2}, \tag{7}$$

with parameters defined as $\alpha = (2A^2 - B)/\sqrt{4A^2+B^2}$, $beta = B/\sqrt{4A^2+B^2}$, $A = \sqrt{(0.5(\gamma-1)rM_e^2/F}$, $B = (1 + 0.5(\gamma-1)rM_e^2 - F)/F$, and $F = T_w/T_e$.

Using the Reynolds analogy, the heat flux, q_w, into the flow from the wall can be calculated as

$$q_w = \rho_e U_e C_p (T_w - T_r)C_{\mathrm{he}}, \tag{8}$$

where the Stanton number is $C_{\mathrm{he}} = C_f/(2Pr^{2/3})$ (White 2006).

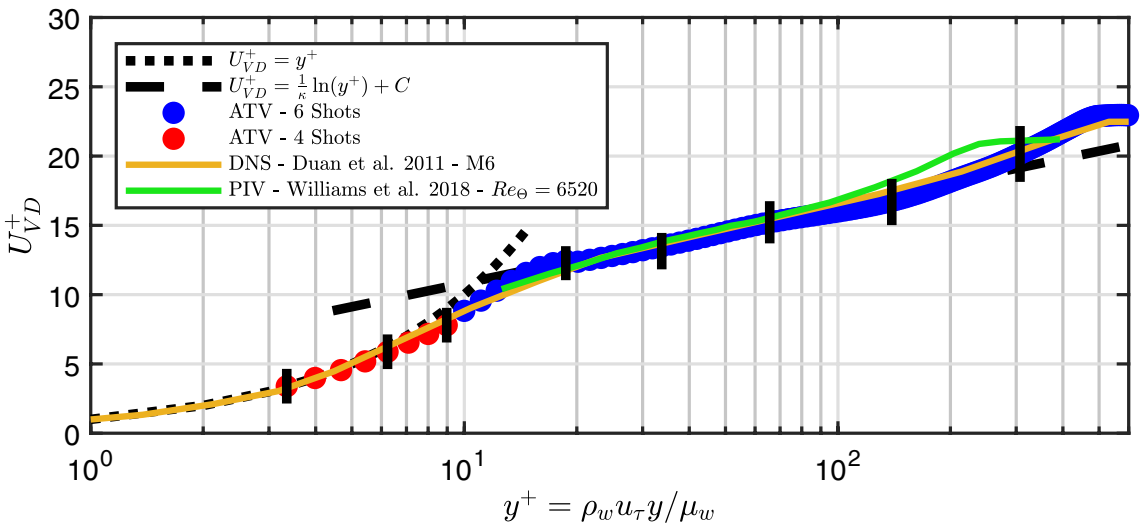

Fig. 12 Van Driest non-dimensionalization of ATV data and comparison to DNS in Duan et al. (2011) and PIV in Williams et al. (2018). Vertical black lines are error estimate for ATV data

The non-dimensionalized ATV data are plotted for all six shots (555 realizations) for $y^+ > 10$ and for four shots (377 realizations) for $y^+ > 3$ in Fig. 12. Two shots were excluded because, in those experiments, the laser-induced breakdown and reflections precluded near-wall measurement. Also included are data from the literature, DNS calculations from Duan et al. (2011) and PIV measurements from Williams et al. (2018) at conditions similar to those reported in Table 2. The error bars of the current ATV data overlap with existing data in the literature. Discrepancies among the data sets are greatest in the wake region which could be Reynolds number dependent.

The Morkovin (1962) scaling of the streamwise velocity fluctuations is presented in Fig. 13. This scaling, which was intended to account for the density variation in the boundary layer, is also compared against data from the literature, again from Duan et al. (2011) and Williams et al. (2018). In Fig. 13, the streamwise fluctuations between the present experiments and the literature match well for the subset of 4 experiments above $y^+ > 10$ ($y/\delta > 0.03$). However, the fluctuations reported for $3 < y^+ < 10$ ($y/\delta < 0.03$) do not appear to be physical or follow the trends in the literature. We assert that, in the current experiments, there is noise arising from the measurement technique which artificially increases the reported fluctuation level but does not appear to affect the mean. Additionally, we note that, near the wall, u'_{RMS} is the difference between a smaller instantaneous velocity and its mean; and therefore, the associated error with tagging velocimetry is larger (see Eq. (2)). The noise from the measurement technique is the result of laser reflections and small laser-induced breakdown at the model surface. For $y/\delta > 1$, the fluctuations do not trend to zero due to (a) camera jitter, which is ≈ 20 ns (less than half of the $\widetilde{\Delta t} =$ 47.5 ns uncertainty in time used to determine the error bars in Eq. (2)) and (b) decreased SNR at and above the boundary-layer edge because the laser was not as focused here.

In Table 3, we present some of the relevant length scales in the flow in the context of some of the length scales of the measurement technique to bring confidence in the presentation of results for the mean velocity profile into the viscous sublayer of a hypersonic turbulent boundary layer. Specifically, the scales of the lowest measurement point and the overlap region are compared to the camera resolution and the calculated beam waist diameter. The relation between y_m and y is found in Eq. (1) and illustrated in Fig. 7. The mapping of y_m to y appreciably stretches the boundary layer out, especially at the wall, as Shekhtman (2022) Section 3.1 showed via a Taylor series expansion that $y \approx y_m^2/(2R_c)$ for $y_m/R < 1$ and $y_w \approx 0$. This stretching alleviates concerns that beam waist and camera resolution are on the same order of the measurand. The uncertainty in determining y from recorded images as in Fig. 7 and processed with Eq. (1) is estimated as

$$\widetilde{y} = \sqrt{\left(\widetilde{\Delta R_c}\frac{\partial y}{\partial R_c}\right)^2 + \left(\widetilde{\Delta y_w}\frac{\partial y}{\partial y_w}\right)^2 + \left(\widetilde{\Delta y_m}\frac{\partial y}{\partial y_m}\right)^2}. \quad (9)$$

Here, we estimate that the uncertainty in the HCF radius is $\widetilde{\Delta R_c} = 0.001$ in (25.4 μ m) from doubling the machining tolerance. The uncertainty in the recorded location of where the laser strikes the HCF is estimated to be $\widetilde{\Delta y_w} = 134$ μ m (within 2 pixels). The uncertainty in the measured image coordinate is estimated to be $\widetilde{\Delta y_m} = 134$ μ m (within 2 pixels). The spanwise location of where the laser strikes the HCF is $\sqrt{R^2 - y_w^2}$ (Fig. 7). Assuming this location is known

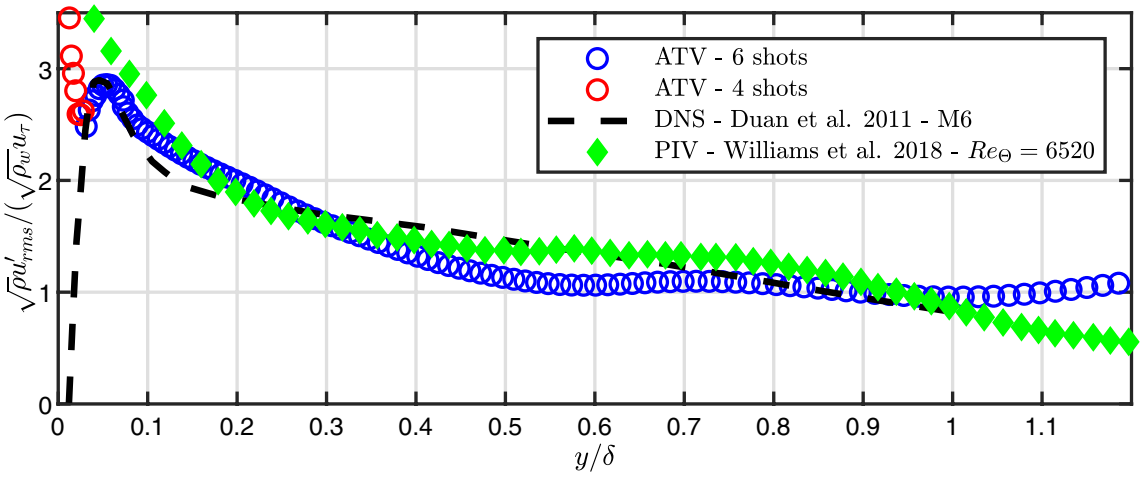

Fig. 13 Morkovin scaling of ATV data of streamwise fluctuations, u'_{RMS}, and comparison to the DNS data in Duan et al. (2011) and PIV data in Williams et al. (2018)

Table 3 Flow and measurement technique length scales

	y μm	y_m μm	y/δ	y^+
Lowest $\overline{u}$ Measurement	100	1400	0.01	3
Overlap Region	300	3300	0.03	10
Camera Resolution at $y_m = 0$	< 10	67/pix	< 0.001	< 0.3
Beam Waist at $y_m = 0$	< 10	68	< 0.001	< 0.3

to within 500 μm (that is, the spanwise location of where the laser strikes the HCF) the uncertainty in the transformed wall-normal coordinate is $\widetilde{y} = 20$ μm.

5 Conclusion

Acetone tagging velocimetry (ATV) with nominally 1% mole fraction acetone seeding was conducted in a shock-tunnel-generated hypersonic turbulent boundary layer over a hollow-cylinder flare at $M_e = 6.05$, $T_w/T_r = 0.65$, $\mathrm{Re}_\theta = 8925$, and $\mathrm{Re}_\tau = 408$. This single-laser tagging velocimetry experiment, which recorded mean and fluctuating streamwise velocity ($\overline{u}$ and u'_{RMS}), had a repetition rate of 50 kHz and did not require the use of an image intensifier. Results are presented for six experiments at nominally the same run condition. The measured velocity at the boundary-layer edge is in good agreement with the freestream velocity calculated with the Stevens Shock Tunnel run-condition calculation procedure.

The ATV data are non-dimensionalized via the van Driest transformation and compared to literature with DNS data from Duan et al. (2011) and PIV measurements from Williams et al. (2018). For all six shots at $y^+ > 10$ (555 realizations), the velocity compares well with the literature, and for four shots (377 realizations), velocity was reported down to $y^+ \approx 3$; this is into the viscous sublayer. Two shots were excluded because, in those experiments, the laser-induced breakdown and reflections precluded near-wall measurement. The Morkovin-scaled fluctuations matched the literature for $y^+ > 10$; however, below $y^+ \approx 10$, it appears that the noise introduced by the measurement technique, in addition to the velocity differences being small near the wall, rendered the ATV-measured Morkovin-scaled fluctuations below $y^+ = 10$ not useful.

Future work involves designing an experiment to measure the wall-normal velocity and fluctuation level, as this is difficult to measure with particle-based methods (Brooks et al. 2018; Aultman et al. 2022); also, tunnel conditions, such as reservoir enthalpy, could be altered to expand the parameter space. Manipulating the photophysics of acetone with an additional CW laser, as is done with certain applications of other tagging techniques, could be performed to increase the tracer lifetime, increase SNR, and decrease required laser-pulse energy. Of technical interest will be efforts to increase the frequency and pulse count from the burst-mode laser to get statistics out of a single experiment. Additionally, methods to more accurately control and reduce the acetone seeding are worthy efforts.

Acknowledgements We thank Eric Marineau and the Office of Naval Research for sponsoring the construction and development of the Stevens Shock Tunnel. We also thank AFOSR program manager Sarah Popkin for her support. We would additionally like to thank our summer scholars Jett Langhorn, Logan Lewis, and Nicholas Oblonsky as well as Bergen County Technical High School intern Yhara Barba for their assistance with the shock tunnel.

Author Contributions All authors have contributed equally.

Funding Ben A. Segall, David Shekhtman, Ahsan Hameed, James H. Chen, and Nicholaus J. Parziale were supported by ONR and AFOSR Grants, including N00014-19-1-2523, N00014-20-1-2637, N00014-20-1-2549, FA9550-16-1-0262, FA9550-18-1-0403, and FA9550-19-1-0182.

Availability of data and materials The datasets generated during the current study are available from the corresponding author on reasonable request.

Declarations

Conflict of interest The authors declare that they have no conflicts of interest and no competing interests.

Ethical approval Not applicable.

References

Andrade A, Hoffman ENA, LaLonde EJ et al (2022) Velocity measurements in a hypersonic flow using acetone molecular tagging velocimetry. Opt Express 30(23):42,199-42,213. https://doi.org/10.1364/OE.474841

André MA, Bardet PM, Burns RA et al (2017) Characterization of hydroxyl tagging velocimetry for low-speed flows. Meas Sci Technol 28(8):085,202. https://doi.org/10.1088/1361-6501/aa7ac8

Aultman MT, Disotell K, Duan L (2022) The effect of particle lag on statistics of hypersonic turbulent boundary layers subject to pressure gradients. In: Proceedings of AIAA Scitech 2022. AIAA-2022-1062, San Diego, California and Virtual, https://doi.org/10.2514/6.2022-1062

Balla RJ (2013) Iodine tagging velocimetry in a Mach 10 wake. AIAA J 51(7):1–3. https://doi.org/10.2514/1.J052416

Bathel BF, Danehy PM, Inman JA et al (2011) Velocity profile measurements in hypersonic flows using sequentially imaged fluorescence-based molecular tagging. AIAA J 49(9):1883–1896. https://doi.org/10.2514/1.J050722

Blitz MA, Heard DE, Pilling MJ (2006) Study of acetone photodissociation over the wavelength range 248–330 nm: evidence of a mechanism involving both the singlet and triplet excited states. J Phys Chem 110:6742–6756. https://doi.org/10.1021/jp056276g

Boedeker LR (1989) Velocity measurement by H_2O photolysis and laser-induced fluorescence of OH. Opt Lett 14(10):473–475. https://doi.org/10.1364/OL.14.000473

Brooks JM, Gupta AK, Helm C, et al (2017) Mach 10 PIV flow field measurements of a turbulent boundary layer and shock turbulent boundary layer interaction. In: Proceedings of the 33rd AIAA aerodynamic measurement technology and ground testing conference. AIAA-2017-3325, Denver, Colorado. https://doi.org/10.2514/6.2017-3325

Brooks JM, Gupta AK, Smith MS et al (2018) Particle image velocimetry measurements of Mach 3 turbulent boundary layers at low Reynolds numbers. Exp Fluids 59:83. https://doi.org/10.1007/s00348-018-2536-x

Browne S, Ziegler J, Shepherd JE (2006) Numerical solution methods for shock and detonation jump conditions. GALCIT - FM2006-006, Caltech

Clark A, McCord W, Zhang Z (2022) Air resonance enhanced multiphoton ionization tagging velocimetry. Appl Opt 61(13):3748–3753. https://doi.org/10.1364/AO.455216

Danehy PM, Weisberger J, Johansen C, et al (2018) Non-intrusive measurement techniques for flow characterization of hypersonic wind tunnels. In: Flow characterization and modeling of hypersonic wind tunnels (NATO science and technology organization lecture series STO-AVT 325). NF1676L-31725 - Von Karman Institute, Brussels, Belgium

Danehy PM, O'Byrne S, Houwing AFP et al (2003) Flow-tagging velocimetry for hypersonic flows using fluorescence of nitric oxide. AIAA J 41(2):263–271. https://doi.org/10.2514/2.1939

Danis ME, Durbin P (2022) Compressibility correction to $\kappa-\omega$ models for hypersonic turbulent boundary layers. AIAA J 60(11):6225–6234. https://doi.org/10.2514/1.J062027

Duan L, Beekman I, Martin MP (2011) Direct numerical simulation of hypersonic turbulent boundary layers. Part 3: effect of Mach number. J Fluid Mech 672:245–267. https://doi.org/10.1017/S0022112010005902

Edwards MR, Dogariu A, Miles RB (2015) Simultaneous temperature and velocity measurements in air with femtosecond laser tagging. AIAA J 53(8):2280–2288. https://doi.org/10.2514/1.J053685

Fratantonio D, Rojas-Cárdenas M, Mohand HSH et al (2018) Molecular tagging velocimetry for confined rarefied gas flows: Phosphorescence emission measurements at low pressure. Exp Therm Fluid Sci 99:510–524. https://doi.org/10.1016/j.expthermflusci.2018.08.001

Goodwin DG (2003) An open-source, extensible software suite for CVD process simulation. In: Allendorf M, Maury F, Teyssandier F (eds), Proceedings of CVD XVI and EuroCVD fourteen, pp 155–162

Gordon S, McBride B (1999) Thermodynamic data to 20000 K for monatomic gases. NASA TP-1999-208523

Gragston M, Smith CD (2022) 10 kHz molecular tagging velocimetry in a Mach 4 air flow with acetone vapor seeding. Exp Fluids 63(85):1–9. https://doi.org/10.1007/s00348-022-03438-1

Handa T, Masuda M, Kashitani M et al (2011) Measurement of number densities in supersonic flows using a method based on laser-induced acetone fluorescence. Exp Fluids 50:1685–1694. https://doi.org/10.1007/s00348-010-1029-3

Handa T, Mii K, Sakurai T et al (2014) Study on supersonic rectangular microjets using molecular tagging velocimetry. Exp Fluids 55:1725. https://doi.org/10.1007/s00348-014-1725-5

Hill RB, Klewicki JC (1996) Data reduction methods for flow tagging velocity measurements. Exp Fluids 20(3):142–152. https://doi.org/10.1007/BF00190270

Holden MS, Wadhams TP, MacLean MG, et al (2013) Measurements in regions of shock wave/turbulent boundary layer interaction from Mach 3 to 10 for open and "blind" code evaluation/validation. AFRL-OSR-VA-TR-2013-0134

Holden MS, Wadhams TP, MacLean MG (2014) Measurements in regions of shock wave/turbulent boundary layer interaction from Mach 4 to 10 at flight duplicated velocities to evaluate and improve the models of turbulence in CFD codes. Tech. rep, CUBRC

Huang PG, Coleman GN (1994) Van driest transformation and compressible wall-bounded flows. AIAA J 32(10):2110–2113. https://doi.org/10.2514/3.12259

Huang J, Duan L, Choudhari MM (2022) Direct numerical simulation of hypersonic turbulent boundary layers: effect of spatial evolution and Reynolds number. J Fluid Mech 937:A3. https://doi.org/10.1017/jfm.2022.80

Jiang N, Halls BR, Stauffer HU et al (2016) Selective two-photon absorptive resonance femtosecond-laser electronic-excitation tagging velocimetry. Opt Lett 41(10):2225–2228. https://doi.org/10.1364/OL.41.002225

Jiang N, Mance JG, Slipchenko MN et al (2017) Seedless velocimetry at 100 kHz with picosecond-laser electronic-excitation tagging. Opt Lett 42(2):239–242. https://doi.org/10.1364/OL.42.000239

Jiang N, Hsu PS, Gragston M et al (2023) Recent progress in high-speed laser diagnostics for hypersonic flows. Appl Opt 62(6):A59–A75. https://doi.org/10.1364/AO.480298

Jiang N, Hsu PS, Grib SW et al (2023) Mach 18 flow velocimetry with 100-kHz KTV and PLEET in AEDC Tunnel 9. Appl Opt 62(6):A25–A30. https://doi.org/10.1364/AO.477203

Khalil AAI, Richardson M, Barnett C et al (2006) Double pulse UV laser induced breakdown spectroscopy of stainless steel. J Appl Spectrosc 73(5):735–742. https://doi.org/10.1007/s10812-006-0147-4

Korte JJ, Lafferty JF, Smith MS, et al (2021) Determination of hypervelocity freestream conditions for a vibrationally frozen nitrogen flow. In: Proceedings of AIAA SciTech 2021. AIAA-2021-0981, Virtual Event. https://doi.org/10.2514/6.2021-0981

Laderman AJ, Demetriades A (1974) Mean and fluctuating flow measurements in the hypersonic boundary layer over a cooled wall. J Fluid Mech 63(1):121–144. https://doi.org/10.1017/S0022112074001042

Lempert WR, Jiang N, Sethuram S et al (2002) Molecular tagging velocimetry measurements in supersonic microjets. AIAA J 40(6):1065–1070. https://doi.org/10.2514/2.1789

Lempert WR, Boehm M, Jiang N et al (2003) Comparison of molecular tagging velocimetry data and direct simulation Monte Carlo simulations in supersonic micro jet flows. Exp Fluids 34(3):403–411. https://doi.org/10.1007/s00348-002-0576-7

Leyva IA (2017) The relentless pursuit of hypersonic flight. Phys Today 70(11):30–36. https://doi.org/10.1063/PT.3.3762

Loth E (2008) Compressibility and rarefaction effects on drag of a spherical particle. AIAA J 46(9):2219–2228. https://doi.org/10.2514/1.28943

Lozano A (1992) Laser-excited luminescent tracers for planar concentration measurements in gaseous jets. PhD thesis, Stanford University

McBride BJ, Zehe MJ, Gordon S (2002) NASA Glenn coefficients for calculating thermodynamic properties of individual species. NASA TP-2002-211556

McDaniel JC, Hiller B, Hanson RK (1983) Simultaneous multiple-point velocity measurements using laser-induced iodine fluorescence. Opt Lett 8(1):51–53. https://doi.org/10.1364/OL.8.000051

Michael JB, Edwards MR, Dogariu A et al (2011) Femtosecond laser electronic excitation tagging for quantitative velocity imaging in air. Appl Opt 50(26):5158–5162. https://doi.org/10.1364/AO.50.005158

Mills JL (2016) Investigation of multi-photon excitation in argon with applications in hypersonic flow diagnostics. PhD thesis, Old Dominion University

Mirzaei M, Dam NJ, van der Water W (2012) Molecular tagging velocimetry in turbulence using biacetyl. Phys Rev E 86(4):1–8. https://doi.org/10.1103/PhysRevE.86.046318

Morkovin MV (1962) Effects of compressibility on turbulent flows. Mécanique de la Turbulence pp 367–380. CNRS

Mustafa MA , Parziale NJ (2017a) Krypton tagging velocimetry in the stevens shock tube. In: Proceedings of 33rd AIAA aerodynamic measurement technology and ground testing conference. AIAA-2017-3897, Denver, Colorado. https://doi.org/10.2514/6.2017-3897

Mustafa MA, Hunt MB, Parziale NJ, et al (2017b) Krypton Tagging Velocimetry (KTV) Investigation of shock-wave/turbulent boundary-layer interaction. In: Proceedings of AIAA SciTech 2017. AIAA-2017-0025, Grapevine, Texas. https://doi.org/10.2514/6.2017-0025

Mustafa MA, Parziale NJ, Smith MS, et al (2018) Two-Dimensional Krypton Tagging Velocimetry (KTV-2D) Investigation of shock-wave/turbulent boundary-layer interaction. In: Proceedings of AIAA SciTech 2018. AIAA-2018-1771, Kissimmee, Florida. https://doi.org/10.2514/6.2018-1771

Mustafa MA, Parziale NJ (2018) Simplified read schemes for krypton tagging velocimetry in N_2 and air. Opt Lett 43(12):2909–2912. https://doi.org/10.1364/OL.43.002909

Mustafa MA, Parziale NJ, Smith MS et al (2017) Nonintrusive freestream velocity measurement in a large-scale hypersonic wind tunnel. AIAA J 55(10):3611–3616. https://doi.org/10.2514/1.J056177

Mustafa MA, Parziale NJ, Smith MS et al (2019) Amplification and structure of streamwise-velocity fluctuations in compression-corner shock-wave/turbulent boundary-layer interactions. J Fluid Mech 863:1091–1122. https://doi.org/10.1017/jfm.2018.1029

Mustafa MA, Shekhtman D, Parziale NJ (2019) Single-laser krypton tagging velocimetry investigation of supersonic Air and N_2 boundary-layer flows over a hollow cylinder in a shock tube. Phys Rev Appl 11(6):064,013. https://doi.org/10.1103/PhysRevApplied.11.064013

Neeb D, Saile D, Gülhan A (2018) Experiments on a smooth wall hypersonic boundary layer at Mach 6. Exp Fluids 59:68. https://doi.org/10.1007/s00348-018-2518-z

O'Haver T (1997) A pragmatic introduction to signal processing. University of Maryland at College Park

Parziale NJ, Smith MS, Marineau EC (2015) Krypton tagging velocimetry of an underexpanded jet. Appl Opt 54(16):5094–5101. https://doi.org/10.1364/AO.54.005094

Pitz RW, Lahr MD, Douglas ZW et al (2005) Hydroxyl tagging velocimetry in a supersonic flow over a cavity. Appl Opt 44(31):6692–6700. https://doi.org/10.1364/AO.44.006692

Sato K, Hidaka Y (2000) Shock-Tube and modeling study of acetone pyrolysis and oxidation. Combust Flame 22:291–311. https://doi.org/10.1016/S0010-2180(00)00121-8

Schulz C, Sick V (2005) Tracer-LIF diagnostics: quantitative measurement of fuel concentration, temperature and fuel/air ratio in practical combustion systems. Progress Energy Combust Sci 31:75–121. https://doi.org/10.1016/j.pecs.2004.08.002

Shekhtman D (2022) Multiphoton processes for high-speed optical diagnostics. PhD thesis. https://www.proquest.com/docview/2685491627/40CFF10876D547AFPQ/1?accountid=14052

Shekhtman D, Mustafa MA, Parziale NJ (2020) Two-photon cross-section calculations for krypton in the 190–220 nm range. Appl Opt 59(34):10826–10837. https://doi.org/10.1364/AO.410806

Shekhtman D, Yu WM, Mustafa MA et al (2021) Freestream velocity-profile measurement in a large-scale, high-enthalpy reflected-shock tunnel. Exp Fluids 62(118):1–13. https://doi.org/10.1007/s00348-021-03207-6

Shekhtman D, Hameed A, Segall BA, et al (2022) initial shakedown testing of the stevens shock tunnel. In: Proceedings of AIAA SciTech 2022. AIAA 2022-1402, San Diego, California and Virtual Event. https://doi.org/10.2514/6.2022-1402

Smits AJ, Matheson N, Joubert PN (1983) Low-Reynolds-number turbulent boundary layers in zero and favorable pressure gradients. J Ship Res 27(03):147–157. https://doi.org/10.5957/jsr.1983.27.3.147

Tran TT (2008) Acetone planar laser-induced fluorescence and phosphorescence for mixing studies of multiphase flows at high pressure and temperature. PhD thesis, Georgia Institute of Technology

Tran T, Kochar Y, Seitzman J (2005) Measurements of liquid acetone fluorescence and phosphorescence for two-phase fuel imaging. In: Proceedings of 43rd aerospace sciences meeting and exhibit. AIAA-2005-0827, Reno, Nevada. https://doi.org/10.2514/6.2005-827

Tropea C, Yarin AL, Foss JF (2007) Springer handbook of experimental fluid mechanics. Springer, Berlin

Walz A (1959) Compressible turbulent boundary layers with heat transfer and pressure gradient in flow direction. J Res Natl Bur Stand-B 63B(1):53–70. https://doi.org/10.6028/jres.063B.008

Wehrmeyer JA, Ribarov LA, Oguss DA et al (1999) Flame flow tagging velocimetry with 193-nm H_2O photodissociation. Appl Opt 38(33):6912–6917. https://doi.org/10.1364/AO.38.006912

White F (2006) Viscous fluid flow, 3rd edn. McGraw-Hill, New York

Williams OJH, Sahoo D, Baumgartner ML et al (2018) Experiments on the structure and scaling of hypersonic turbulent boundary layers. J Fluid Mech 834:237–270. https://doi.org/10.1017/jfm.2017.712

Yu D, Tian Z, Wang Z et al (2018) Estimation of enthalpy of bio-oil vapor and heat required for pyrolysis of biomass. Fuel 234:1380–1387. https://doi.org/10.1016/j.fuel.2018.08.020

Zahradka D, Parziale NJ, Smith MS et al (2016) Krypton tagging velocimetry in a turbulent Mach 2.7 boundary layer. Exp Fluids 57:62. https://doi.org/10.1007/s00348-016-2148-2